JACS
JOURNAL OF THE AMERICAN CHEMICAL SOCIETY

ARTICLE

pubs.acs.org/JACS

Polyoxometalate-Based Metal Organic Frameworks (POMOFs): Structural Trends, Energetics, and High Electrocatalytic Efficiency for Hydrogen Evolution Reaction

Brigitte Nohra,[†] Hani El Moll,[†] L. Marleny Rodriguez Albelo,[‡] Pierre Mialane,[†] Jérôme Marrot,[†] Caroline Mellot-Draznieks,[*,§] Michael O'Keeffe,[∥] Rosa Ngo Biboum,[⊥] Joël Lemaire,[#] Bineta Keita,[*,⊥] Louis Nadjo,[⊥] and Anne Dolbecq[*,†]

[†]Institut Lavoisier de Versailles, UMR 8180, Université de Versailles Saint-Quentin en Yvelines, 45 Avenue des Etats-Unis, 78035 Versailles cedex, France

[‡]Zeolite Engineering Laboratory, Institute of Materials Research and Engineering (IMRE), University of Havana, Havana, 10400, Cuba

[§]Laboratoire de Chimie et Biologie des Métaux, Université Joseph Fourier, Grenoble, Centre National de la Recherche Scientifique, Unité Mixte de Recherche 5249, CEA, DSV/iRTSV, 17 rue des Martyrs, F-38054, Grenoble cedex 9, France

[∥]Department of Chemistry and Biochemistry, Arizona State University, Tempe, Arizona 85287, United States

Laboratoire de Chimie Physique, [⊥]Groupe d'Electrochimie et de Photoélectrochimie, and [#]Groupe Ions en Phase Gazeuse, UMR 8000, CNRS, Université Paris-Sud, Bâtiment 350, 91405 Orsay cedex, France

Supporting Information

ABSTRACT: The grafting of the triangular 1,3,5-benzene tricarboxylate linkers (denoted trim) on tetrahedral ε-Keggin polyoxometalates (POMs) capped by Zn(II) ions, formed in situ under hydrothermal conditions, has generated three novel POM-based metal organic frameworks (POMOFs). $(TBA)_3[PMo^{V}_{8}Mo^{VI}_{4}O_{36}(OH)_4Zn_4][C_6H_3(COO)_3]_{4/3}\cdot 6H_2O$ ($\boldsymbol{\varepsilon}$**(trim)**$_{4/3}$) is a 3D open-framework built of molecular Keggin units connected by trim linkers, with channels occupied by tetrabutylammonium (TBA) counterions. $\boldsymbol{\varepsilon}$**(trim)**$_{4/3}$ is a novel (3,4)-connected net, named **ofp** for open-framework polyoxometalate, and computer simulations have been used to evaluate its relative stability in comparison with **ctn**- and **bor**-like polymorphs, showing the stability of this novel phase directly related to its greatest density. A computational study was also undertaken with the aim of locating TBA molecules, the positions of which could not be deduced from single crystal X-ray diffraction, and further rationalizes their structure directing role. In $(TBA)_3[PMo^{V}_{8}Mo^{VI}_{4}O_{37}(OH)_3Zn_4][C_6H_3(COO)_3]$ ($\boldsymbol{\varepsilon}_2$**(trim)**$_2$), the building unit is not the molecular Keggin but a dimerized form of this POM. Their connection via trim linkers generates a 3D framework with channels filled by TBA cations. In $(TBA)_3[PMo^{V}_{8}Mo^{VI}_{4}O_{37}(OH)_3Zn_4][C_6H_3(COO)_3]\cdot 8H_2O$ ($[\boldsymbol{\varepsilon}$**(trim)**$]_\infty$), zigzag chains are connected via the organic linkers, forming 2D grids. Modified electrodes were fabricated by direct adsorption of the POMOFs on glassy carbon or entrapment in carbon paste (CPE). A remarkable electrocatalytic hydrogen evolution reaction (HER) was detected with a yield greater than 95%, and a turnover number as high as 1.2×10^5 was obtained after 5 h. The reported POMOF-based electrodes are more active than platinum, with a roughly 260 mV anodic shift. Finally, the electrocatalytic activities of $\boldsymbol{\varepsilon}$**(trim)**$_{4/3}$/CPE electrodes in various XCl (X = Li, Na, K, Cs) media have been studied. This allowed us to detect a cation effect and propose an electrocatalytic mechanistic pathway for the HER.

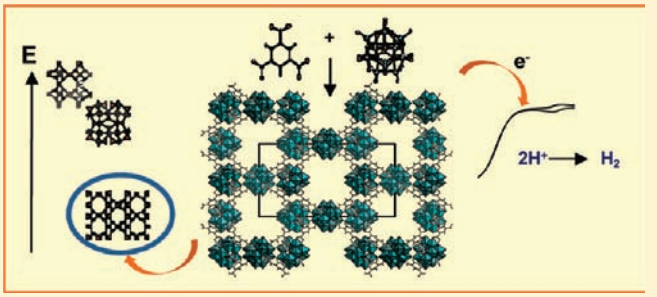

INTRODUCTION

In the rapidly developing context of hybrid framework materials or metal organic frameworks (MOFs),[1] polyoxometalates (POMs), a large family of soluble anionic metal oxide clusters of d-block transition metals in high oxidation states (W^{VI}, $Mo^{V,VI}$, $V^{IV,V}$), constitute ideal building blocks for targeting new multifunctional materials[2] due to their wide range of magnetic,[3] redox,[4] and catalytic properties.[5] On the one hand, the assembly of Keggin type ions,[6] ring-shaped POMs[7] with redox active transition metal ions, or polyoxovanadate clusters[8] into purely inorganic extended molecular frameworks is fueling the current incentive for the design of functional materials from POMs. On the other hand, the range of available hybrid frameworks has

Received: February 7, 2011
Published: July 21, 2011

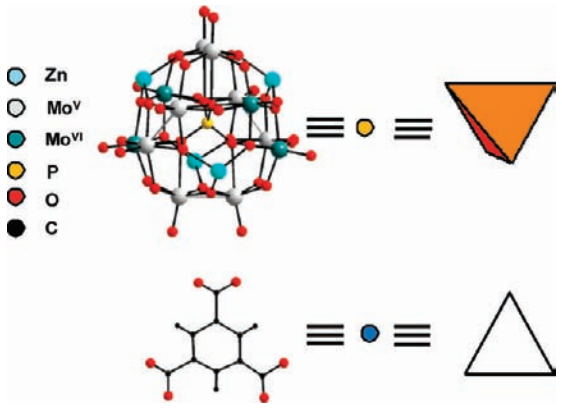

Figure 1. Ball-and-stick representation of the $\{\varepsilon\text{-}PMo^{V}{}_{8}Mo^{VI}{}_{4}O_{36}(OH)_{4}Zn_{4}\}$ Keggin core and of the trim linker and their schematic representation: an orange sphere represents the center of mass of the POM and a blue sphere the center of mass of the organic linker; the Zn-ε-Keggin core can also be schematized as an orange tetrahedron (the vertices of the tetrahedron are occupied by the Zn ions) and the trimesate linker by a triangle (the vertices are occupied by the carbon atoms of the carboxylate groups).

exploded in the last 10 years and using "Chimie Douce"[9] methods or hydrothermal syntheses.[10] Recently has emerged a new class of POM-based MOFs, so-called POMOFs,[11] built from the connection of POMs to one another through bridging organic linkers.

The properties and diverse coordination modes of POMs together with the diversity of organic linkers provide an impetus for the synthesis of multifunctional materials. For example, magnetic conductors combining the magnetic properties of POMs and electric properties of tetrathiafulvalene or perylene derivatives[12] or electroactive hybrids based on POMs and conducting organic polymers have been reported.[13] The extensive electrochemical activity of molecular POMs may also be further exploited if they can be retained in an insoluble framework, opening avenues in fields such as sensors or electrocatalysis, a research area still in its infancy in the field of MOFs.[14] While a growing number of extended POMOFs with a diversity of topologies[15] have been described, 3D POMOF frameworks are less common. For example, enantiomerically pure 3D POMOFs have been synthesized by reaction of $[BW_{12}O_{40}]^{5-}$, Cu^{II}, and D- or L-proline in water[16] where the chiral proline transfers chirality to the achiral Keggin POM via the Cu^{II} ions. An open framework with perovskite topology has also been recently reported[17] as well as Keggin type POMs connected by silver[18] or copper[19] complexes.

We have developed for a few years a new family of POMOFs using ε-Keggin (Figure 1) POMs as building blocks. This POM has the general formula $\{\varepsilon\text{-}PMo^{V}{}_{8}Mo^{VI}{}_{4}O_{40-x}(OH)_{x}M_{4}\}$ (M = Zn^{II}, La^{III}) and contains an ε-Keggin core capped by four M metallic ions. The overall charge of the ε-Keggin results from the number of protonated oxo bridging linkers, which may vary from 0 to 5. These Keggin entities are therefore versatile building blocks that may be used either as anions (M = Zn, $x = 0$) or cations (M = Zn, La, $x = 3-5$).[20−22] The ε-Keggin ion has a remarkable ability to successfully react with a variety of organic linkers such as bipyridine,[21b,22,23] benzenedicarboxylic acid (BDC),[24] or imidazole.[25] Specifically, the Zn-ε-Keggin caught our attention because it possesses a tetrahedral shape in which four Zn^{II} cations are exposed in a regular tetrahedral arrangement in a fashion similar to oxygen atoms in SiO_4 tetrahedra. Connecting these tetrahedral Zn-ε-Keggins together with bidentate linkers, a combined simulation-synthetic strategy allowed us to generate zeolite-like POMOFs. Among all simulated polymorphs, the diamond-like structure was predicted as the most stable one and further synthesized as Z-POMOF-1, $[NBu_4]_3[PMo^{V}{}_{8}Mo^{VI}{}_{4}O_{36}(OH)_{4}Zn_{4}(BDC)_{2}]\cdot 2H_2O$, an electroactive triply interpenetrated network.[24]

Here, we explore a new family of extended POMOFs turning to the tridentate 1,3,5 benzene tricarboxylate linkers, or trimesate (denoted here trim), keeping the Zn-ε-Keggin as the inorganic building blocks. The targeted combination of tetrahedral inorganic building blocks and rigid triangular organic linkers is expected to produce (3,4)-connected nets such as those identified by O'Keeffe with the **bor** and **ctn** network,[26] as recently exemplified by the synthesis of **bor**-like[27−29] or **ctn**-like framework materials.[30] Still, it is striking that there are only a few examples of hybrid frameworks adopting (3,4)-connected nets. We may stipulate that the occurrence of such (3,4)-connected nets as MOFs is rendered difficult by the limited availability of building blocks with exactly the desired shapes. Moreover, the control of their further assembly with a strict alternation of triangular and tetrahedral building blocks required for producing these topologies is obviously a synthetic challenge. Here again, simulations were used to support our experimental synthetic strategy, with the purpose of simulating possible polymorphs and ranking them in terms of lattice energies. Inspired by the reticular chemistry concepts,[31] we have used a "decoration"[32,33] strategy of adimensional nets, in a fashion similar to that previously used for the ZIFs[34] (zinc imidazole frameworks) family, and performed force field geometry optimizations.

We describe herein the synthesis and characterizations of a series of novel POMOFs containing monomeric, dimeric, or chain-like Zn-ε-Keggin building blocks connected by trimesate ions. Special emphasis is put on the discovery of a novel (3,4)-connected net, **ofp**, for open-framework polyoxometalate, $\boldsymbol{\varepsilon}$-$(\mathbf{trim})_{4/3}$, a 3D POMOF with channels. Computer simulations are further used to evaluate the relative stability of $\boldsymbol{\varepsilon}(\mathbf{trim})_{4/3}$ in comparison with its **ctn**- and **bor**-like polymorphs. The impact of the TBA (tetrabutylammonium) template molecules in the stabilization of $\boldsymbol{\varepsilon}(\mathbf{trim})_{4/3}$ and their potential role as structure directing agent is also discussed. The electrochemical properties of the three materials are compared, and the electrocatalytic performances of $\boldsymbol{\varepsilon}(\mathbf{trim})_{4/3}$-based electrodes for hydrogen evolution reaction are highlighted.

METHODS

Synthesis and Characterizations. Hydrothermal syntheses were carried out in 23 mL polytetrafluoroethylene-lined stainless steel containers under autogenous pressure. Commercially available reagents were used as received, without further purification. All reactants were stirred briefly before heating. The mixture was heated to 180 °C over a period of 1 h, kept at 180 °C for 40 h, and cooled to room temperature over a period of 88 h. The pH mixture was measured before (pH_i) and after the reaction (pH_f). The products were isolated by filtration and washed with ethanol.

Preparation of $(TBA)_3[PMo^{V}{}_{8}Mo^{VI}{}_{4}O_{36}(OH)_{4}Zn_{4}][C_6H_3(COO)_3]_{4/3}\cdot 6H_2O$ ($\boldsymbol{\varepsilon}(\mathbf{trim})_{4/3}$): A mixture of $(NH_4)_6Mo_7O_{24}\cdot 4H_2O$ (0.618 g, 0.50 mmol), molybdenum powder 99.99% (0.060 g, 0.62 mmol), H_3PO_3 (0.020 g, 0.25 mmol), zinc chloride (0.136 g, 1 mmol), 1,3,5 benzenetricarboxylic

Table 1. Crystallographic Data for $\varepsilon(\text{trim})_{4/3}$, $\varepsilon_2(\text{trim})_2$, and $[\varepsilon(\text{trim})]_\infty$

	$\varepsilon(\text{trim})_{4/3}$	$\varepsilon_2(\text{trim})_2$	$[\varepsilon(\text{trim})]_\infty$
empirical formula	$C_{60}H_{128}Mo_{12}N_3O_{54}P$	$C_{57}H_{114}Mo_{12}N_3O_{46}P$	$C_{57}H_{128}Mo_{12}N_3O_{54}P$
formula weight, g	3199.38	3021.34	3165.35
crystal system	orthorhombic	orthorhombic	orthorhombic
space group	*I*222	*Pnnm*	*Pmma*
a/Å	21.6212(10)	24.156(9)	17.779(10)
b/Å	22.5502(10)	24.992(9)	16.388(9)
c /Å	42.1069(17)	16.214(6)	16.204(9)
V/Å^3	20529.7(16)	9788(6)	4721(5)
Z	6	4	2
ρ_{calc}/g cm^{-3}	1.553	2.022	2.212
μ/mm^{-1}	1.825	2.537	2.642
data/parameters	18 304/523	7417/333	4478/168
R_{int}	0.0695	0.1145	0.1601
GOF	0.915	0.966	0.985
R ($>2\sigma(I)$)	$R_1{}^a$ = 0.0442	$R_1{}^a$ = 0.0785	$R_1{}^a$ = 0.0834
	$wR_2{}^b$= 0.1242	$wR_2{}^b$= 0.1928	$wR_2{}^b$= 0.2232

^{a} $R_1 = (\Sigma|F_o| - |F_c|)/(\Sigma|F_c|)$. ^{b} $wR_2 = ((\Sigma w(F_o^2 - F_c^2)^2)/(\Sigma w(F_o^2)^2))^{1/2}$.

acid (0.210 g, 1 mmol), tetrabutylammonium hydroxide 40 wt % solution in water (160 μL, 0.24 mmol), and H_2O (12 mL) was stirred, and the pH was adjusted to 5 (pH_i) with 2 M HCl (pH_f = 4.8). Dark red cubic crystals suitable for X-ray diffraction study were collected after filtration (0.155 g, 20% based on P). Anal. Calcd for $C_{60}H_{128}Mo_{12}N_3O_{54}PZn_4$: C, 22.52; H, 4.03; Mo, 35.98; N, 1.31; P, 0.97; Zn, 8.17. Found: C, 22.83; H, 3.95; Mo, 37.98; N, 1.39; P, 1.04; Zn, 8.27. IR (KBr pellets, ν/cm^{-1}): 2961 (s), 2931 (s), 2873 (s), 2623 (sh), 2348 (m), 1962 (w), 1638 (m), 1619 (m), 1579 (sh), 1573 (m), 1481 (m), 1482 (m), 1461 (m), 1381(sh), 1357 (m), 1209 (m), 1167 (w), 1147 (w), 1063 (w), 1020 (m), 965 (m), 940 (s), 814 (s), 786(s), 764 (m), 745 (s), 708 (s), 592 (s), 549 (m), 520 (m), 486 (m).

Preparation of $(TBA)_3[PMo^V{}_8Mo^{VI}{}_4O_{37}(OH)_3Zn_4][C_6H_3(COO)_3]$ (ε_2**(trim)$_2$**): A mixture of $Na_2MoO_4 \cdot 4H_2O$ (0.847 g, 3.50 mmol), molybdenum powder 99.99% (0.060 g, 0.62 mmol), H_3PO_3 (0.020 g, 0.25 mmol), zinc chloride (0.136 g, 1 mmol), 1,3,5 benzenetricarboxylic acid (0.210 g, 1 mmol), tetrabutylammonium hydroxide 40 wt % solution in water (160 μL, 0.24 mmol), and H_2O (12 mL) was stirred, and the pH was adjusted to 5 (pH_i) with 2 M HCl (pH_f = 4.8). Dark red platelets suitable for X-ray diffraction study were collected after filtration (0.122 g, 16% based on P). Anal. Calcd for $C_{57}H_{114}Mo_{12}N_3O_{46}PZn_4$: C, 22.66; H, 3.80; Mo, 38.10; N, 1.39; P, 1.02; Zn, 8.66. Found: C, 23.56; H, 3.91; Mo, 37.97; N, 1.29; P, 0.96; Zn, 8.08. IR (KBr pellets, ν/cm^{-1}): 2958 (s), 2933 (s), 2872 (s), 2348 (m), 1720 (w), 1617 (m), 1573 (m), 1471 (m), 1450 (sh), 1381(sh), 1356 (s), 1148 (w), 1062 (w), 984 (m), 960 (m), 939 (s), 816 (s), 776(s), 711 (m), 620 (w), 592 (s), 535 (m), 518 (m), 482 (m).

Preparation of $(TBA)_3[PMo^V{}_8Mo^{VI}{}_4O_{37}(OH)_3Zn_4][C_6H_3(COO)_3]\cdot 8H_2O$ ($[\varepsilon$**(trim)**$]_\infty$): A mixture of $Na_2MoO_4 \cdot 4H_2O$ (0.847 g, 3.50 mmol), molybdenum powder 99.99% (0.060 g, 0.62 mmol), H_3PO_3 (0.020 g, 0.25 mmol), zinc chloride (0.136 g, 1 mmol), 1,3,5 benzenetricarboxylic acid (0.210 g, 1 mmol), tetrabutylammonium hydroxide 40 wt % solution in water (160 μL, 0.24 mmol), and H_2O (9 mL) was stirred, and the pH was adjusted to 5 (pH_i) with 2 M HCl (pH_f = 4.8). Red platelets suitable for X-ray diffraction study were collected after filtration (0.097 g, 12% based on P). Anal. Calcd for $C_{57}H_{130}Mo_{12}N_3O_{54}PZn_4$: C, 21.63; H, 4.10; Mo, 36.38; N, 1.33; P, 0.98; Zn, 8.26. Found: C, 19.74; H, 3.49; Mo, 36.15; N, 1.10; P, 0.94; Zn, 8.45. IR (KBr pellets, ν/cm^{-1}): 2961 (s), 2932 (s), 2848 (s), 2349 (m), 2299 (m), 1638 (w), 1620 (m), 1579 (sh), 1573 (w), 1481 (m), 1450 (sh), 1381(sh), 1358 (s), 1148 (w), 1062 (w), 965 (m), 939 (s), 816 (s), 783 (s), 709 (m), 592 (s), 540 (m), 518 (m), 482 (m).

Infrared spectra were recorded on an FTIR Magna 550 Nicolet spectrophotometer as pressed KBr pellets.

Data collections were carried out using a Siemens SMART three-circle diffractometer for all of the structures except for $\varepsilon(\text{trim})_{4/3}$ for which data were collected using a Bruker Nonius X8 APEX 2 diffractometer. Both were equipped with a CCD bidimensional detector using the monochromatized wavelength λ(Mo Kα) = 0.71073 Å. Absorption correction was based on multiple and symmetry-equivalent reflections in the data set using the SADABS program[35] based on the method of Blessing.[36] The structure was solved by direct methods and refined by full-matrix least-squares using the SHELX-TL package.[37] For all three structures, the cations could not be located in the structure due to severe disorder, and the data set was corrected with the program SQUEEZE,[38] a part of the PLATON package of crystallographic software used to calculate the solvent or counterions disorder area and to remove its contribution to the overall intensity data. Crystallographic data are given in Table 1, and a CIF file is available free of charge via the Internet at http://pubs.acs.org.

Powder diffraction data were obtained on a Brüker D5000 diffractometer using Cu radiation (1.54059 Å). Temperature-dependent X-ray diffraction was performed on a Siemens D-5000 diffractometer in the $\theta-\theta$ mode under air using Co radiation (1.79021 Å). Each pattern was recorded with a 2 s per step scan, which gave an approximate scan time of 1 h for each pattern at any given temperature. The heating rate between two temperatures was 5 °C min^{-1}.

Energetics of the ***ofp****-like* ε***(trim)*$_{4/3}$** *and Its* ***ctn****- and* ***bor****-like Polymorphs.* We considered the model derived from the experimental crystal structure of the **ofp**-like POMOF, $\varepsilon(\text{trim})_{4/3}$. Two other polymorphs of $\varepsilon(\text{trim})_{4/3}$ were constructed. The combination of triangles and tetrahedra with a strict alternation, like that observed in $\varepsilon(\text{trim})_{4/3}$, gives rise to (3,4)-connected networks such as **ctn** or **bor** nets.[39] For the purpose of comparison between the three polymorphs, the TBA molecules and the intra-POM PO_4 species were not included, keeping the {ε-Keggin, trim} skeleton only and ensuring its neutrality as detailed below. The mineral boracite is a magnesium chloroborate, $Mg_3B_7O_{12}Cl$, and possesses a (3,4)-connected net based on corner-sharing BO_3 triangles and BO_4 tetrahedra. The **ctn** topology is that proposed as a hypothetical C_3N_4. We used our so-called "decoration" strategy[32,33] to construct the **ctn**- and **bor**-like $\varepsilon(\text{trim})_{4/3}$, using an upper-scale unit cell of the parent inorganic net and placing the Zn-ε Keggin and the trim linker on the tetrahedral and triangular nodes, respectively. Both the organic and the inorganic building blocks were inserted in the appropriate orientation so that the symmetry of the parent net is preserved. It is important to note here that both nets require the insertion of only one type of building block, that is, one trimesate and one Zn-ε-Keggin per asymmetric unit, in their respective space group, *I*-43*d* and *P*-43*m*. The **bor**- and **ctn**-like POMOFs were subsequently geometry optimized as summarized here.

All three models, that is, the experimental **ofp**-like $\varepsilon(\text{trim})_{4/3}$ and its **bor**- and **ctn**-like polymorphs, were subjected to geometry optimization in *P*1 to determine the equilibrium structures at constant pressure and their relative lattice energies. Because our models have a very large number of atoms (each ε-Keggin and trim linker possess 57 and 21 atoms, respectively), geometry optimization using a molecular mechanics forcefield is the only feasible route at this stage. Our choice of the so-called universal forcefield, *uff*,[40] is dictated by the need to consider a range of element types (Mo, Zn, O, C, H) and bonding types. Bond parameters for describing Zn−O bonds were modified to reproduce the Zn−O distances typically observed in the experimental $\varepsilon(\text{trim})_{4/3}$ POMOF at ~2 Å. In that purpose, we varied the atomic radius of Zn to 1.453 Å to obtain the required bond length. We further constrained the simulations, given the concerns about the transferability of the

interatomic potentials for such systems. The ε-Keggin and the trim linker were treated as rigid bodies, while the Zn−O bonds that ensure the interbuilding blocks connections were free to relax. Assigning such rigid motion groups has the advantage of preserving the complex geometry of the ε-Keggin, while allowing the ε-Keggin and the trim linker to reorient relative to one another, providing the required framework flexibility. The nonbonded interactions between pairs of atoms are represented by Lennard-Jones potentials, calculated in real space within relevant cutoffs, plus a Coulombic term, evaluated by the Ewald summation to describe the electrostatics. The atomic charges for each model were calculated by the charge−equilibrium method,[41] and the average value was then taken and fixed for all three structures, so that the same set of charges was used throughout and artifact variations of the electrostatic term among the three polymorphs were thus avoided. The minimized lattice energy of each model was normalized to the number of POMs per unit cell in the structure.

Docking of TBA in $\boldsymbol{\varepsilon(trim)_{4/3}}$. The lack of experimental evidence on the location of TBA counterions in $\boldsymbol{\varepsilon(trim)_{4/3}}$ is a common feature, resulting from resolution limitations. Calculations were performed to provide a model for the location of template TBA molecules in the pores and investigate their stabilizing role. Here, we may assume that the host−guest interactions occur mainly between the organic TBA molecules, on the one hand, and the peripheral oxygen atoms of the ε-Keggin building block, on the other hand, neglecting short-range interactions with the metal centers of the ε-Keggin due to their confinement. Here, molecular structures and interactions energies of the TBA molecules within the $\boldsymbol{\varepsilon(trim)_{4/3}}$ framework were described using the *cvff* forcefield, validated for the simulation of organic molecules.[42] An increasing number of TBA molecules were sequentially inserted in the porous $\boldsymbol{\varepsilon(trim)_{4/3}}$ framework in *P*1 through a conventional "docking" procedure, selecting the most favorable configurations through a simulated annealing procedure. This procedure was first validated by the correct prediction of the location of TBA molecules in the related compound $(TBA)_3[PMo^{V}_8Mo^{VI}_4O_{36}(OH)_4Zn_4(BDC)_2].2H_2O$ (Z-POMOF1)[24] for which a full structure solution was at hand (Figure SI1). At this stage, only short-range interactions were computed. The hybrid framework was kept rigid, while TBA molecules were left free to relax. The selected docked positions of TBA obtained in *P*1 were transformed into the closest symmetric positions compatible with *I*222, the space group of the $\boldsymbol{\varepsilon(trim)_{4/3}}$ structure. Once the maximum number of TBA molecules were inserted, all TBA molecules were geometry optimized, including electrostatics this time, keeping the framework fixed and using partial charges calculated from the charge−equilibration method.[43] Four TBA sites were identified (I, II, III, and IV), providing a total of 16 molecules per unit cell among the 18 TBA molecules present in $\boldsymbol{\varepsilon(trim)_{4/3}}$. Finally, the net short-range stabilization provided by each of the four sites, named TBA_i, was estimated as follows:

$$\Delta E(TBA_i) = E(\text{total}) - E(\text{total} - TBA_i) - E(TBA_i)$$

where $E(\text{total})$ refers to the energy of $\boldsymbol{\varepsilon(trim)_{4/3}}$ containing all TBA molecules, $E(\text{total} - TBA_i)$ refers to the energy of $\boldsymbol{\varepsilon(trim)_{4/3}}$ containing all TBA molecules except TBA_i, and $E(TBA_i)$ represents the energy of the periodic subnetwork of TBA_i molecules. The energy variation $\Delta E(TBA_i)$ is normalized by the number of TBA molecules in site *i* per unit cell and may be considered as the short-range stabilization energy emanating from TBA_i template molecules. The electrostatic contribution of each type of TBA_i to $\Delta E(TBA_i)$ could not be easily estimated due to the non additive nature of Coulombic interactions. All calculations were performed using Materials Studio suite of software.[43] The results are reported in Table 3.

Electrochemical Studies. The solutions were deaerated thoroughly for at least 30 min with pure argon and kept under a positive pressure of this gas during the experiments. The electrochemical setup was an EG&G 273 A driven by a PC with the M270 software. Potentials are quoted against a saturated calomel electrode (SCE). The counter electrode was a platinum gauze of large surface area. All experiments were performed at room temperature.

The composition of the various aqueous media was as follows: for pH 0, 1 M LiCl + HCl; for pH 1, 1 M XCl (X = Li^+, Na^+, K^+, or Cs^+) + HCl; and for pH 2−3, 1 M LiCl + HCl.

Electrode Preparation. Two immobilization methods were used to assess solid-state electrochemical behavior of the POMOFs: The first was POMOF-CPEs (POMOF carbon paste modified electrodes). Carbon paste electrodes (CPEs) were prepared as previously described.[24] Typically, the carbon paste was obtained by thoroughly hand-mixing mineral oil (Aldrich) with 50 mg of Vulcan XC-72 (Cabot Corp.) and 2 mg of POMOF. A portion of the paste was packed into a glass tube (3 mm inner diameter), and the inner surface of this paste cylinder was pressed against a copper wire. The electrode surface was smoothed with a soft surface. The second was direct adsorption of POMOF-Vulcan XC-72 on glassy carbon (POMOF-GC) electrode with a literature method.[44] First, a mixture containing 15 mg of Vulcan XC-72 and the desired amount of POMOF (1, 2, or 3 mg) was cogrounded. Next, a few microliters of an aqueous suspension of this mixture was deposited onto the GC electrode, and allowed to dry in air at room temperature. The assembly was covered with 5 wt % Nafion solution and again allowed to dry in air at room temperature. The volume content of the Nafion is 25% of the suspension volume.

Chronoamperometric Evidence for Lithium Intercalation on the Second Wave of $\boldsymbol{\varepsilon(trim)_{4/3}}$*/CPE.* The following experiments provide compelling evidence of lithium intercalation into the POMOF network and the corresponding potential dependence. For this purpose, the $\boldsymbol{\varepsilon(trim)_{4/3}}$/CPE system associated with a (1 M LiCl + HCl (pH 1)) medium was selected. Figure SI2 summarizes the relevant observations. The chronoamperometric current of the first two-electron wave of the POMOF decreases steadily from its initial value, thus displaying classical behavior (Figure SI2). In contrast, a more complex variation of the chronoamperometric current was observed to occur as soon as the potential was stepped to reach the second voltammetric wave. The phenomenon manifests itself in the following way: an initial current decrease is followed by an increase featuring a nucleation process and finally a monotonous decrease is observed (Figure SI2). An analogous chronoamperometric pattern was described in the literature.[45] Specifically, the current increase was associated with a nucleation process during lithium ions insertion into graphite. This experimental evidence establishes the existence of a lithium ion intercalation process commencing at the foot of the second wave and running along this wave. The same phenomena were observed with POMOF-GC electrodes.

Hydrogen Analysis. The gas sample composition was analyzed using a quadrupole mass analyzer (SRS model RGA300). The available mass over charge range goes from m/z 1 to 300. Because no ions were observed at high masses, the spectrum are shown in the range m/z 1−65. Ionization is performed by electron impact with electron energy of 70 eV and a 1 mA electron current. The vacuum chamber housing the mass spectrometer was pumped by a 70 L/s turbomolecular pump backed by a scroll primary pump. The pressure in the chamber is measured by a cold cathode gauge (Pfeifer model PKR251). The background vacuum prior to sample introduction was 1.7×10^{-8} mbar (consisting mostly of water and hydrogen) and can be neglected because the pressure during sample introduction was set close to 10^{-5} mbar.

RESULTS AND DISCUSSION

Structures. The inorganic building block of $\boldsymbol{\varepsilon(trim)_{4/3}}$ is the well-known $\{\varepsilon\text{-}PMo^{V}_8Mo^{VI}_4O_{36}(OH)_4Zn_4\}$ POM (Figure 1). In this POM, the electrons are localized in $Mo^{V}-Mo^{V}$ bonds. Accordingly, the $Mo^{V}\cdots Mo^{V}$ distances are equal to ∼2.6 Å and

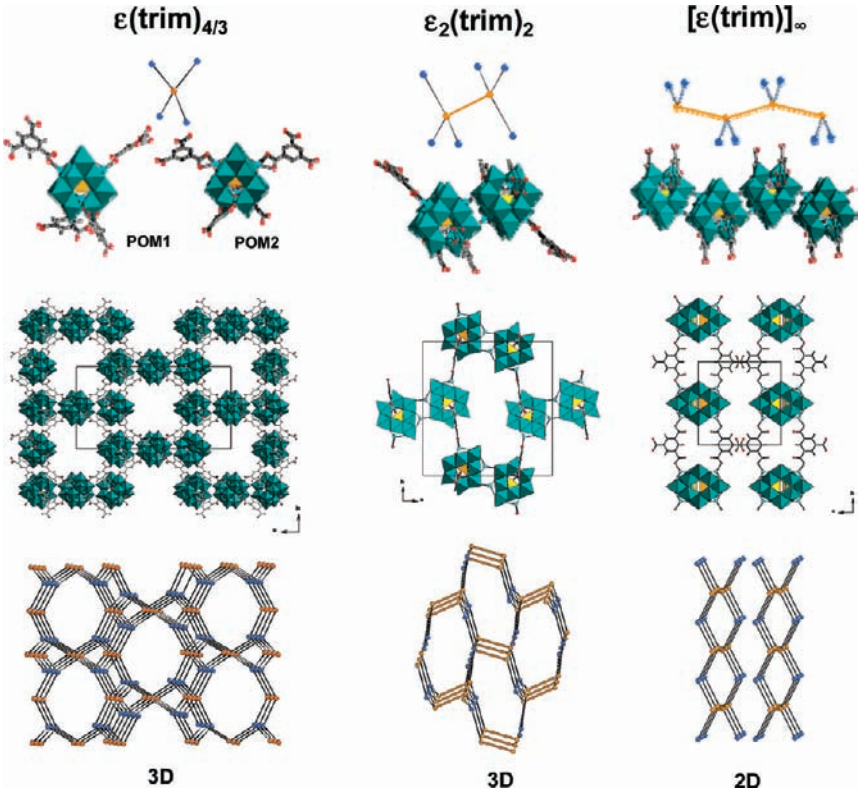

Figure 2. POM building blocks of $\boldsymbol{\varepsilon}(\mathbf{trim})_{4/3}$, $\boldsymbol{\varepsilon}_2(\mathbf{trim})_2$, and $[\boldsymbol{\varepsilon}(\mathbf{trim})]_\infty$, a view of their unit cell, and their schematic representation; black lines indicate connections between POMs and trim linkers, while orange lines symbolize condensation reactions between POMs.

$Mo^{VI}\cdots Mo^{VI}$ distances to ~3.2 Å, and the compound is red contrarily to POMs with delocalized electrons, the so-called "molybdenum blue species".[46] In $\boldsymbol{\varepsilon}(\mathbf{trim})_{4/3}$, there are two different POMs, POM-1 and POM-2, in the asymmetric unit (Figures 2 and SI3). In POM-1, each capping Zn ion in the tetrahedral environment is bound to three oxygen atoms of the POM and to one oxygen atom of a carboxylate group, which adopts a monodentate coordination mode. In POM-2, the carboxylate groups have bidentate coordination modes, leading thus to pentacoordinated Zn^{II} ions. The three carboxylate groups of the trim linker allow connecting two POM-1 and one POM-2 (Figure SI4). The overall tetrahedral symmetry of the ε-Keggin POM precursor is thus maintained. The connection of these tetrahedral units via trim linkers in the three directions of space affords a 3D material (Figure 2). Examination of the Mo···Mo distances has confirmed the presence of 8 Mo^{V} and 4 Mo^{VI} ions in POM1. Valence bond calculations (Figure SI3) have shown that four bridging oxygen atoms are protonated. This determination has not been possible on POM2 because of disorder. The remaining charges are compensated by TBA cations. The detailed formula of $\boldsymbol{\varepsilon}(\mathbf{trim})_{4/3}$ is thus $(TBA)_3[PMo^{V}_{8}Mo^{VI}_{4}O_{36}(OH)_4Zn_4][C_6H_3(COO)_3]_{4/3}\cdot 6H_2O$. The schematic view of the structure shows clearly the presence of tunnels with an almost spherical aperture, which run along the *a* axis (Figure 2). Channels with slightly smaller apertures along the *b* axis intersect these tunnels (Figure SI5). The TBA counterions and water molecules are supposed to occupy these channels, but their positions could not be determined by X-ray diffraction due to severe disorder. The structure of $\boldsymbol{\varepsilon}(\mathbf{trim})_{4/3}$ constitutes a rare example of a 3D structure with POM units linked by transition metal ions M and organic linkers L following POM−M−L−M−POM sequences. Furthermore, there is no interpenetration like in Z-POMOF1.[24] As a consequence, the solvent-accessible voids calculated by PLATON[47] for the structure without the contribution of TBA amount to the very large value of 14 770 $Å^3$ and represents 72% of the total volume of the structure. This observation has motivated cation exchange experiments to recover some porosity (see below).

Slight changes in the experimental synthetic conditions had strong influences on the structures of the isolated compounds affording two other phases, $\boldsymbol{\varepsilon}_2(\mathbf{trim})_2$ and $[\boldsymbol{\varepsilon}(\mathbf{trim})]_\infty$. The building POM unit of $\boldsymbol{\varepsilon}_2(\mathbf{trim})_2$ is not the expected Zn-ε-Keggin POM but a dimerized form of this POM (Figure 2). In this dimer, two Zn-ε-Keggin units are linked via two Zn−O bonds between one capping Zn ion on a POM and a bridging oxygen atom of a neighboring POM. This dimerization has already been observed in the structure of the imidazolate derivative.[25] Consequently, the POM unit has six anchoring points. The structure of this dimeric unit evokes the staggered conformation of ethane (Figure 2). The connection of the dimeric POMs via trim linkers generates a 3D framework (Figure 2), while only layers were observed in the imidazolate structure because of the presence of a protonated terminal imidazole linker on two among the six Zn^{II} ions.[25] Two of the carboxylate groups of the trim linkers adopt a monodentate coordination mode, and the remaining one has a symmetric bidentate coordination mode (Figure SI6). As in $\boldsymbol{\varepsilon}(\mathbf{trim})_{4/3}$, the POM contains an eight-electron reduced ε-Keggin core (Figure SI7), but the POM/linker ratio is equal to 1 instead of 4/3 because of dimerization. The charge of the framework is compensated by disordered TBA cations and by three protons localized on three bridging oxygen atoms of the

POM, to lead to the detailed formulas $(TBA)_3[PMo^{V}_8Mo^{VI}_4O_{37}(OH)_3Zn_4][C_6H_3(COO)_3]$. The TBA counter-cations fill the rectangular channels running along the *c* axis (Figure 2).

In $[\boldsymbol{\varepsilon}(\mathbf{trim})]_\infty$, the POM building block is the zigzag chain $\{PMo^{V}_8Mo^{VI}_4O_{37}(OH)_3Zn_4\}_\infty$ (Figure 2), which can be seen as the condensation of $\{PMo^{V}_8Mo^{VI}_4O_{37}(OH)_3Zn_4\}$ POMs via Zn−O bonds with two adjacent POMs, and not only one like in $\boldsymbol{\varepsilon_2}(\mathbf{trim})_2$. Such condensation has previously been evidenced in the chain built of molybdogermanate ε-Keggin POMs $\{GeMo^{V}_8Mo^{VI}_4O_{36}(OH)_4Ni_4\}$.[33] In $[\boldsymbol{\varepsilon}(\mathbf{trim})]_\infty$, four Zn^{II} positions remain available to coordinate to monodentate organic linkers, thus generating a 2D grid with zigzag chains connected via a double bridge of trim linkers (Figure 2). The third position on the trim linker remains non coordinated (Figure SI8). Valence bond calculations confirm the presence of protons on bridging oxygen atoms (Figure SI9).

Synthesis and Characterizations. The synthesis of $\boldsymbol{\varepsilon}(\mathbf{trim})_{4/3}$, $\boldsymbol{\varepsilon_2}(\mathbf{trim})_2$, and $[\boldsymbol{\varepsilon}(\mathbf{trim})]_\infty$ was performed by the reaction of a Mo^{VI} precursor, Mo as reducing agent, H_3PO_3, $ZnCl_2$, 1,3,5 benzenetricarboxylic (trimesic) acid, and TBAOH in water at 180 °C. These conditions are known to generate in situ the $\{\varepsilon\text{-}PMo^{V}_8Mo^{VI}_4O_{36}(OH)_4Zn_4\}$ core.[21b,25] The synthetic conditions are very close for the three phases (Table 2), the differences between them being the nature of the Mo^{VI} precursor, the volume of water, and the temperature. At 200 °C, $\boldsymbol{\varepsilon}(\mathbf{trim})_{4/3}$ is the only phase that crystallizes. As observed for Z-POMOF1,[24] the value of the initial pH (around 5.0) is critical, as is the presence of the TBA cations. Attempts to replace these cations with smaller alkaline or ammonium ions during the synthesis process have so far failed, suggesting that these bulky ions act not simply as counterions but also as structure-directing agents. The three compounds are isolated as dark red insoluble crystals in moderate yield. The purity of the phases has been checked by comparison of the experimental X-ray powder pattern with the powder pattern calculated from the structure solved from single-crystal X-ray diffraction data (Figure SI10). The thermal stability of the three compounds has been investigated by powder X-ray thermal diffraction (Figure SI11). The three phases are stable up to 160 °C.

The infrared spectra of the three phases are similar. Several regions can be distinguished (Figure SI12): the ν_{C-O} vibrations of the carboxylate linker are identified around 1620 and 1570 (ν_{asym}) and 1380 and 1350 cm^{-1} (νs_{ym}). The signature of the TBA cations is found around 1480 cm^{-1}, while the P−O and Mo═O vibrations of the inorganic skeleton of the POM are encountered around 1060 and 940 cm^{-1}, respectively. The Mo−O−Mo vibrations are found below 940 cm^{-1}.

To obtain a porous material, the bulky TBA cations of $\boldsymbol{\varepsilon}(\mathbf{trim})_{4/3}$ must be replaced by smaller cations. As direct syntheses with smaller cations such as Na^+, K^+, NH_4^+, or tetramethylammonium (TMA) have failed, as mentioned above, we have tried to exchange the cations in the raw material. Crystals of $\boldsymbol{\varepsilon}(\mathbf{trim})_{4/3}$ have been suspended in a solution containing chloride salts of smaller cations. The nature of the solvent as well as the concentration and the nature of the counterions have been varied. The cation exchange has been followed by IR spectroscopy. An example of the IR spectrum of the exchange with TMA in H_2O/CH_3CN (50/50) is shown in Figure SI12. After 1 h, the broad lines characteristic of the TBA cations have been replaced by the thinner line of the TMA ions showing the success of cation exchange. However, concomitantly to this exchange, it can be noted a decrease of the intensity of the bands corresponding to the C−O vibrations and a modification of the bands characteristic to the Mo═O vibrations, which suggests some decomposition of the POMOF material. The C−O bands have totally disappeared after 6 h. It has not been possible so far to find suitable experimental conditions in which the POMOF framework is maintained and the TBA are exchanged. The weak monodentate coordination modes of the trimesate probably account for this instability.

Table 2. Precursors and Conditions Used for the Synthesis for $\boldsymbol{\varepsilon}(\mathbf{trim})_{4/3}$, $\boldsymbol{\varepsilon_2}(\mathbf{trim})_2$, and $[\boldsymbol{\varepsilon}(\mathbf{trim})]_\infty$

	$(NH_4)_6Mo_7O_{24}$ 12 mL of H_2O	Na_2MoO_4 12 mL of H_2O	Na_2MoO_4 9 mL of H_2O
180 °C	$\boldsymbol{\varepsilon}(\mathbf{trim})_{4/3}$	$\boldsymbol{\varepsilon_2}(\mathbf{trim})_2$	$[\boldsymbol{\varepsilon}(\mathbf{trim})]_\infty$
200 °C	$\boldsymbol{\varepsilon}(\mathbf{trim})_{4/3}$	$\boldsymbol{\varepsilon}(\mathbf{trim})_{4/3}$	$\boldsymbol{\varepsilon}(\mathbf{trim})_{4/3}$

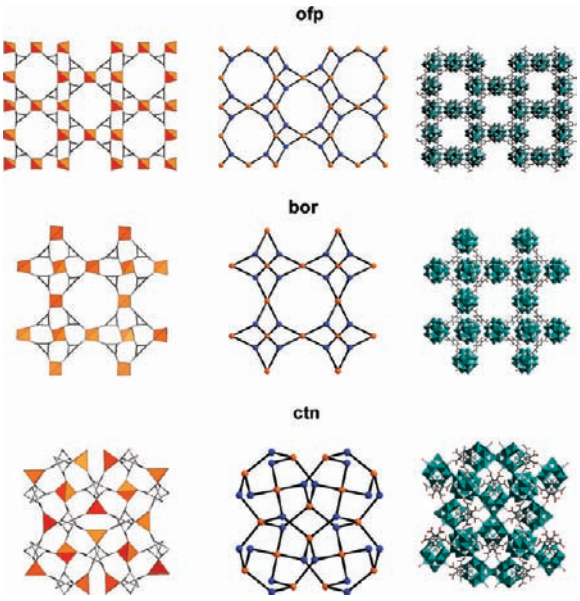

Figure 3. Crystal structures of the three $\boldsymbol{\varepsilon}(\mathbf{trim})_{4/3}$ POMOFs described in the simulation section: the experimental **ofp**-like (top), **bor**-like (middle), and **ctn**-like (bottom) topologies, represented by tetrahedral building blocks and triangular linkers (left structures), nodes (middle structures; tetrahedral nodes in orange, triangular nodes in blue), and their constitutive organic and polyoxometalates building blocks (right structures).

Energetics of ofp-$\boldsymbol{\varepsilon}(\mathbf{trim})_{4/3}$ and Its ctn- and bor-like Polymorphs. In principle, there is an infinite number of (3,4) periodic nets resulting from the linking of tetrahedra with triangles. However, it is known that only a very restricted number of nets might be preferred a priori as "default structure" assuming unbiased synthesis conditions. These preferred nets generally correspond to the most symmetrical ones, and especially to those with just one kind of link, here **ctn** and **bor**.[26] In the present case, it is striking that the **ctn**- (*I*-43*d*) and **bor**-like (*P*-43*m*) nets are not the observed outcomes, but rather the less symmetric $\boldsymbol{\varepsilon}(\mathbf{trim})_{4/3}$ (*I*222), a new net, **ofp** (ideal symmetry *I*-42*m*), as yet unreported in the field of MOFs to our knowledge (Figure 3).

Focusing on topological features, **ctn** and **bor** both possess the minimum number of vertices of each kind (1 tetrahedral site and 1 triangular site) for one kind of edge. By contrast, the **ofp** net exhibits three kinds of vertices (2 tetrahedral sites, 1 triangular

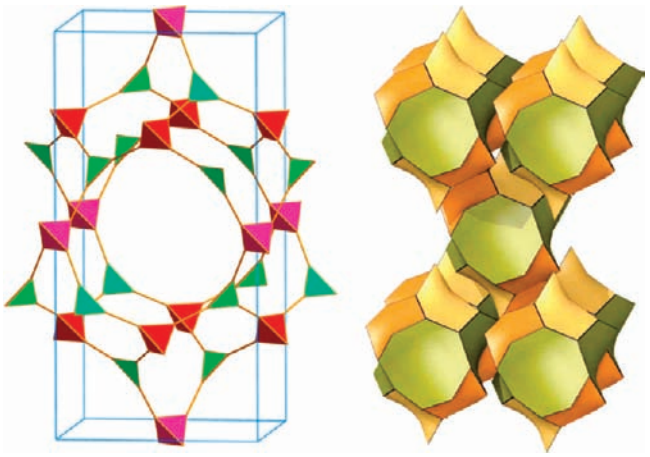

Figure 4. The **ofp** augmented net (left) and its corresponding isohedral tiling (right).

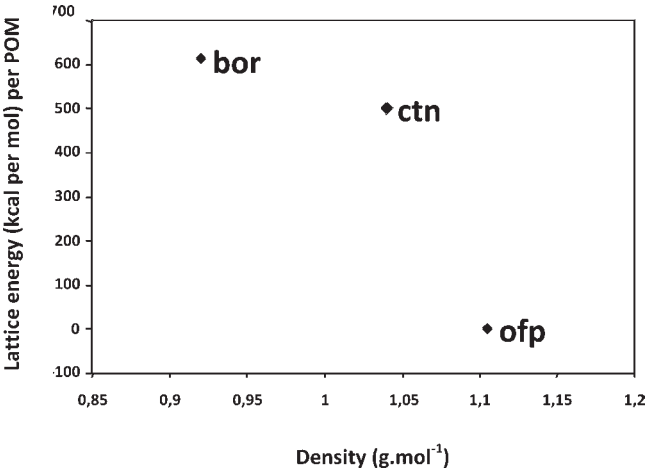

Figure 5. Variation of lattice energies of the three ε(**trim**)$_{4/3}$ polymorphs, **ofp**, **bor**, and **ctn**-like with density expressed as the number of Zn-ε-Keggin per unit cell.

site) with two kinds of edges, the minimum possible number with three kinds of vertices. Figure 4 shows the corresponding augmented net of **ofp** replacing each vertex by its coordination figure, that is, a triangle for a trim linker and a tetrahedron for a Zn-ε Keggin ion. The **ofp** net has just one kind of tile per unit cell, being an isohedral net in contrast with **ctn** and **bor** that require two types of tiles per unit cell (Figure SI13). The requirement of just one tile per primitive unit cell makes the **ofp** topology particularly simple in comparison with that of **ctn** or **bor**, which might be a hint toward its synthetic occurrence.

Turning now to energetic trends (Figure 5), an interesting element of comparison lies in the differences of framework densities: the **ofp**-like ε(**trim**)$_{4/3}$ is notably more dense (1.10 g mol^{-1}) than **ctn**- (1.04 g mol^{-1}) and **bor**-like (0.92 g mol^{-1}) polymorphs. Interestingly, the densest ε(**trim**)$_{4/3}$ is found as the most stable framework, revealing that the relative instability of the **ctn**- and **bor**-like ε(**trim**)$_{4/3}$ may be correlated to their lower density. This is consistent with our previous findings in terms of energy/density trends in zeolite-like families such as ZIFs[34] and Z-POMOFs,[24] found reminiscent of that in zeolites.[48] The present case of ε(**trim**)$_{4/3}$ corroborates our previous findings indicating that thermodynamic control[49] might be at play here by favoring the densest and most stable (3,4)-connected **ofp**-like ε(**trim**)$_{4/3}$.

Model for a Template Directed Assembly of ε(trim)$_{4/3}$. We considered that the nonoccurrence of the default **bor** and **ctn** topologies might point toward the key role of the TBA template. The simplicity of the **ofp** isohedral net might be a clue indicating that templating effect is at play in driving the formation of the **ofp**-like ε(**trim**)$_{4/3}$. The lack of crystallographic data on the location of TBA molecules in open framework materials is an obvious obstacle, however frequent, and usually due to the resolution limitations in the diffraction setup. It is probable that due to the large size of the **ofp** cages and channels, much larger than an individual TBA molecule, structure direction may be at play through the cooperative and complex aggregation of TBA molecules. Thus, docking calculations were done to attempt to locate TBA molecules in the ε(**trim**)$_{4/3}$ and gain insights into the impact of TBA in the stabilization of the **ofp**-like ε(**trim**)$_{4/3}$.

An important result of the simulations is the successful insertion of 16 TBA molecules per unit cell among the 18 ones of ε(**trim**)$_{4/3}$ (Figure 6). Four preferred sites were found, named

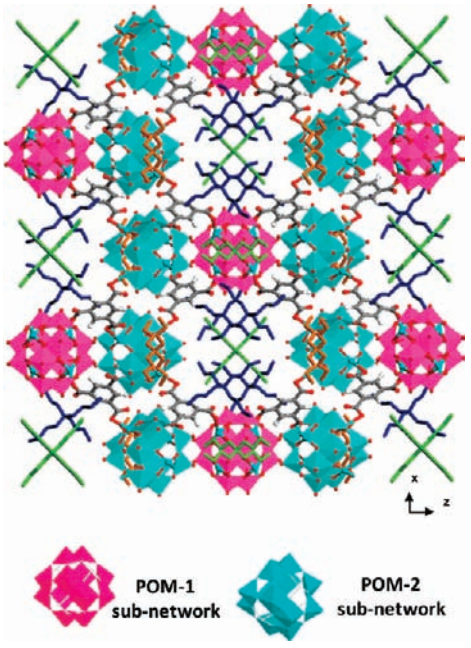

Figure 6. Positions of TBA molecules obtained from simulations within the **ofp**-like ε(**trim**)$_{4/3}$ crystal structure. The skeleton of TBA molecules is represented in either blue, orange, or green.

I, **II**, **III**, and **IV** (Figure 7), which possess distinctive energetic features (Table 3). In total, 2 TBA molecules were located in **I**, 2 in **II**, 4 in **III**, and 8 in **IV** per unit cell. The strength of TBA-framework interactions may be differentiated by (i) the short-range interactions between the TBA molecule and oxygen atoms of the POMOFs through $H_{TBA}\cdots O_{trim}$ or $H_{TBA}\cdots O_{POM}$ interactions, and (ii) the amplitude of the stabilization energy, $\Delta E(TBA_i)$. Distinctions also arise from the type of POMs it interacts with, that is, POM-1 and/or POM-2. TBA in **I** seems to play a distinctive role by templating 4-membered rings of interconnected POMs, with a stabilization energy of −55.5 kcal mol^{-1} per TBA, by far the highest of the four sites. These TBA have interactions with the two subnetworks of POMs, with frequent $H_{TBA}\cdots O_{(POM,trim)}$ contacts at typical distances of

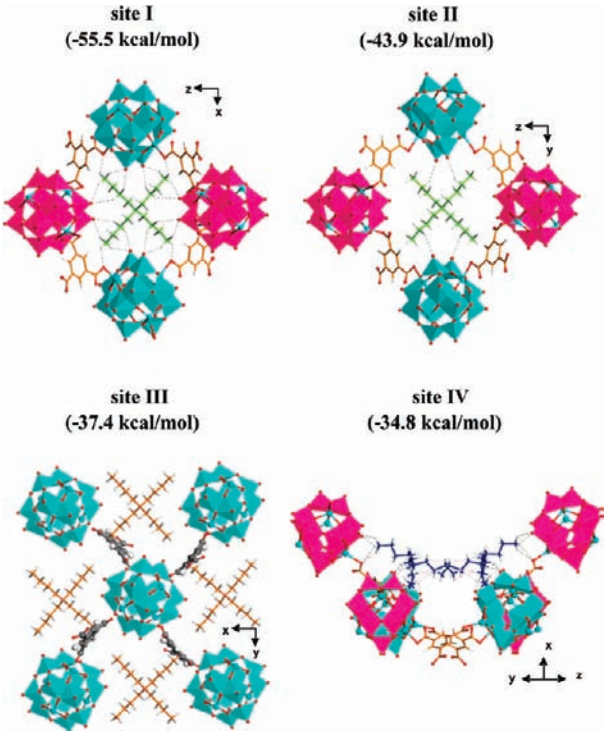

Figure 7. View of the four distinct types of TBA molecules in sites I, II, III, and IV, shown with their respective stabilization energy, $\Delta E(\mathrm{TBA_i})$, normalized per TBA molecule.

2.6−2.9 Å. By contrast, TBA in **II** and **III** molecules interacts less strongly with the POMOF framework, with stabilization energies of −44 and −37.4 kcal mol^{-1} per TBA, respectively. The weakest stabilization energy emanates from the 8 TBA molecules in **IV** (−34.8 kcal mol^{-1} per TBA). They tend to aggregate as dimers within the $\boldsymbol{\varepsilon}(\mathbf{trim})_{4/3}$ structure. These computational results indeed suggest that TBA molecules may play a key structure directing role or a space filling role depending on their location in the channels (Figure SI14). In parallel, the absence of crystallization of $\boldsymbol{\varepsilon}(\mathbf{trim})_{4/3}$ or of any other crystallized form in the absence of TBA is one strong supportive observation of its structure directing role.

Electrochemistry and Hydrogen Evolution Electrocatalysis. Electrochemistry of POMs has been attracting extensive interest due partly to their potential applications in electrocatalytic processes.[50] In this context, various types of POM-based three-dimensional modified electrodes were developed by several groups to circumvent some major drawbacks such as high solubility and low surface area of POMs. Furthermore, on theoretical grounds,[51] the entrapment of POMs in a 3D configuration could induce huge enhancement of their electrocatalytic activity. This trend was termed the "microenvironment effect". However, there are rare examples of experimental evidence of such significant improvement.[52] Because of the structure and insolubility of the POMOFs, they might be anticipated to prove useful in efficient electrocatalysts elaboration. The solid-state electrochemistry of POMOFs was carried out by entrapping them in a carbon paste electrode (CPE), which is a widely used matrix for hybrid electrode materials. Cyclic voltammogram (CV) of $\boldsymbol{\varepsilon}_2(\mathbf{trim})_2$ in a pH 1 medium proceeds through two well-defined Mo-reduction bielectronic waves (Figure 8a) followed by two closely spaced waves (not shown). These

Table 3. Host−Guest van der Waals Interaction Energy in kcal mol^{-1} unit cell^{-1} (Normalized per TBA Molecule) and Structural Features of the Four Different Template Sites in the $\boldsymbol{\varepsilon}(\mathbf{trim})_{4/3}$ Structure

	$\Delta E(\mathrm{TBA_i})$	N(H-bond)/ d(Å)	POM subnetwork	form	$N(\mathrm{TBA_i})$/ uc
site I	−55.5	20/2.6−2.9	POM-2,1 (4-rings)	monomer	2
site II	−43.9	4/2.9	POM-2	monomer	2
site III	−37.4	12/2.7−3	POM-2	monomer	4
site IV	−34.8	9/2.65−3	POM-2,1 (channels)	dimer	8

consecutive electron processes are attributed to the well-known chemically reversible reduction of Mo^{VI} centers.[24] The peak current intensities vary linearly with the scan rate as expected for a surface-controlled process (Figure SI15). The shape of the first redox couples of $\boldsymbol{\varepsilon}(\mathbf{trim})_{4/3}$ and $[\boldsymbol{\varepsilon}(\mathbf{trim})]_\infty$ resembles the one observed for $\boldsymbol{\varepsilon}_2(\mathbf{trim})_2$ in the same experimental conditions. In contrast, their second redox couples present different electrochemical characteristics. Figure 8A shows representative CVs recorded at 100 mV s^{-1} with $\boldsymbol{\varepsilon}(\mathbf{trim})_{4/3}$ or $\boldsymbol{\varepsilon}_2(\mathbf{trim})_2$. The striking observations are the large intensity of the $\boldsymbol{\varepsilon}(\mathbf{trim})_{4/3}$ second reduction wave and the low chemical reversibility of this wave. A decrease of the potential scan rate (v) induces an increase of the ratio R of I_{pc2} to I_{pc1} (I_{pcn} is the reduction peak intensity of the nth wave). Furthermore, the wave becomes chemically irreversible for v < 50 mV s^{-1}. It is worth noting that similar qualitative results are obtained even at scan rates as high as 500 mV s^{-1}. Figure 8B compares the CVs of the three POMOFs recorded at 2 mV s^{-1}. Actually, the same phenomena are observed with $[\boldsymbol{\varepsilon}(\mathbf{trim})]_\infty$ but to a lesser extent. We attribute these observations to an electrocatalytic hydrogen evolution process to be studied in the following. It is worth noting that the electrocatalytic process occurs in the same potential domain for all of the POMOFs, a circumstance that leaves the structures as the main parameters. The intensity of this electrocatalytic process appears to depend on the pH of the supporting electrolyte. The onset potential of this process is driven in the positive direction when the pH decreases. The POMOF/CPE electrodes are remarkably stable and could be cycled hundreds of time without significant alteration (Figure SI16). In addition, these electrodes could be kept for several months in the air, without modification of their behaviors upon soaking in solution. The Mo^{V} centers of these POMOFs are also electroactive. They are associated with a broad plurielectronic irreversible oxidation wave, in agreement with previous CV observations for Z-POMOF1.[24] After oxidation of the Mo^{V} centers, well-behaved CVs are observed. Their peak currents keep varying linearly with the scan rate (Figure 9A). The same electrocatalytic behavior continues to be observed upon reduction of the POMOFs (Figure 9B).

The $\boldsymbol{\varepsilon}(\mathbf{trim})_{4/3}$/CPE system was used for the study of cation effects. Interesting observations are associated with the change of the cations present in the pH 1 supporting electrolyte containing 1 M of alkali cation. In short, the catalytic effect for electrocatalytic hydrogen evolution reaction is still observed with sodium or potassium, albeit with much less intensity than for lithium. Thus, in the lithium-containing electrolyte, the $\boldsymbol{\varepsilon}(\mathbf{trim})_{4/3}$/CPE system is 2.8 and 2.5 times less active when lithium is replaced, respectively, by sodium and potassium.

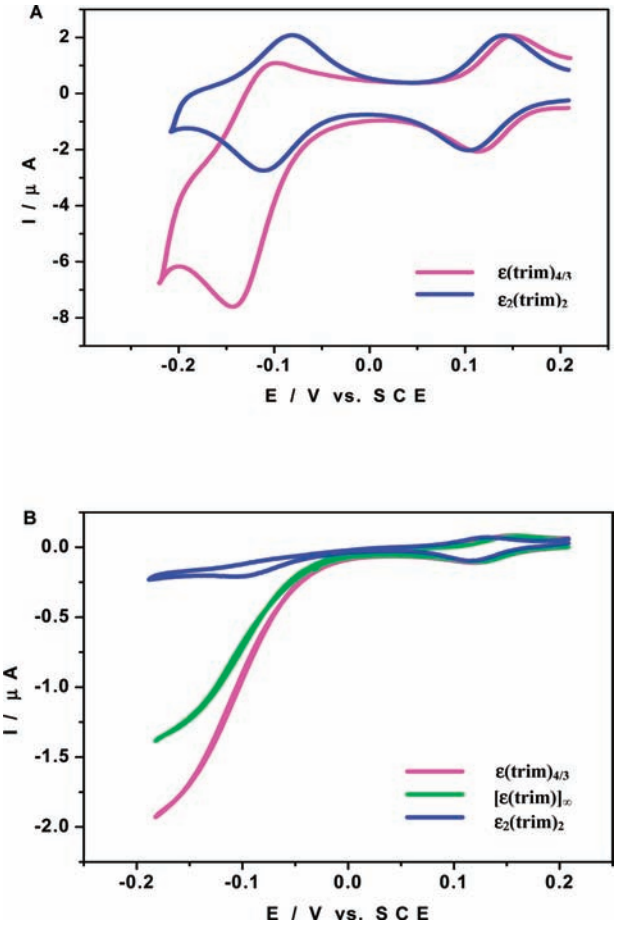

Figure 8. Cyclic voltammograms run in a (1 M LiCl + HCl (pH 1)) medium with the POMOF/CPE assemblies. The reference electrode was SCE. (A) Comparison of $\boldsymbol{\varepsilon}(\mathbf{trim})_{4/3}$ and $\boldsymbol{\varepsilon}_2(\mathbf{trim})_2$ at a scan rate of 100 mV s^{-1}. The reference electrode was a saturated calomel electrode (SCE). (B) Comparison of $\boldsymbol{\varepsilon}(\mathbf{trim})_{4/3}$, $\boldsymbol{\varepsilon}_2(\mathbf{trim})_2$, and $[\boldsymbol{\varepsilon}(\mathbf{trim})]_\infty$ at a scan rate of 2 mV s^{-1}, highlighting the catalytic process. The reference electrode was SCE.

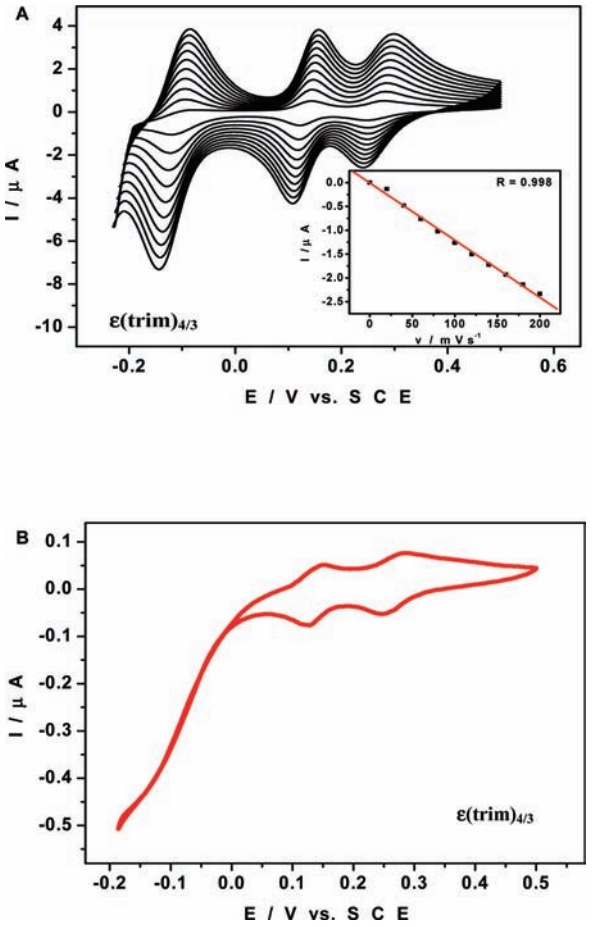

Figure 9. (A) Cyclic voltammograms observed for the oxidized form of $\boldsymbol{\varepsilon}(\mathbf{trim})_{4/3}$/CPE as a function of potential scan rate in a (1 M LiCl + HCl (pH 1)) medium. The scan rate was 100 mV s^{-1}. The reference electrode was a saturated calomel electrode (SCE) (inset: peak current intensity variation of the first reduction wave as a function of scan rate). (B) The same cyclic voltammogram was run at a scan rate of 2 mV s^{-1} to highlight the catalytic process. The reference electrode was SCE.

In contrast, in the presence of a cesium-containing electrolyte, the whole CV undergoes an important alteration upon potential cycling and ends up in a few minutes with a very stable CV (Figure SI17). This rapid transformation is probably due to the instability of $\boldsymbol{\varepsilon}(\mathbf{trim})_{4/3}$ in this medium. Moreover, no catalytic process was detected with the new compound.

Altogether, these observations could be explained by considering both the sizes of the hydrated alkali ions and their propensity to carry water molecules into the POMOF structures. The relative hydrated ionic radii for alkali ions are in the order Li^+ (340 pm)> Na^+ (276 pm) > K^+ (232 pm) > Cs^+ (226 pm). As compared to the radius of the unhydrated TBA (494 pm), hydrated lithium appears as the cation most likely to ensure the cohesion of the POMOF network, which is in agreement with observations. In support of these considerations, it has been shown that lithium insertion occurs on the second wave of the POMOF (Figure SI18). Sodium and potassium show analogous but markedly attenuated trends. Quite the opposite behavior is expected and actually observed with cesium, which is more loosely hydrated. Chronoamperometric experiments provide compelling evidence of lithium intercalation into the POMOF network and the corresponding potential dependence (see experimental section for more details). In addition, the large and firmly hydrated Li^+ ions will carry with them the largest number of water molecules into the structures, a circumstance that is favorable for hydrogen evolution reaction (HER) electrocatalysis. Again, the $\boldsymbol{\varepsilon}(\mathbf{trim})_{4/3}$/CPE system associated with a (1 M LiCl + HCl (pH 1)) medium was kept. The preceding combined cyclic voltammetry and chronoamperometry experiments proved useful in this issue. Altogether, these results would suggest that protonation might prevail in the neutralization of the first reduction wave, while both H^+ and Li^+ should be operating on the second wave. The onset potential of the HER at pH 1 is clearly around +20 mV vs SCE, while the expected onset on a clean Pt electrode is −242 mV vs SCE. In short, a roughly 260 mV anodic shift is observed for the HER. In other words, our electrode assembly is more active than platinum. This behavior might, tentatively, be partly traced to the introduction of proton accepting basic sites in these POMOFs and to the presence of channels in which cations are confined. Even though not very common, related efficiency for the HER is not without precedent in the literature. For example, a molecular catalyst, made of conducting polypyrrole containing ferrocene sulfonate

as counterion, was recently described: with a 270 mV anodic shift in 1 M H_2SO_4, the performances of this electrode exceed those of Pt.[53] Beginning at the potential of the second wave toward more negative values, gas bubbles are generated, featuring an electrocatalytic process. Controlled potential coulometry permitted us to collect this gas, which was then analyzed by direct injection into a quadrupole mass analyzer. Several overpotential values (η) ranging from 0 to 200 mV and a $\boldsymbol{\varepsilon}(\mathbf{trim})_{4/3}$ loading of 3.1×10^{-8} mol cm^{-2} were used for coulometric experiments. Typically, the mass spectrum obtained after an electrolysis at $\eta = 200$ mV is shown in Figure SI19A. The background hydrogen concentration prior to injection is negligible (Figure SI19B). The main components are hydrogen and air. Their relative contributions are evaluated from the peak intensities on the mass spectrum corrected for the different sensitivity factors for H_2 and N_2 and for the difference in the vacuum pumping speed (45 L/s for H_2 and 65 L/s for N_2). The sensitivity factors were determined to be 1.24×10^{-4} A/Torr for N_2 and 2.04×10^{-4} A/Torr for H_2 using pure samples and applying a correction factor of 2.4 to the gauge reading when pure H_2 is introduced. The resulting concentrations in the sample are 47% H_2, 41% N_2, and 11% O_2. As the sample pressure measured with a piezo resistive gauge (Hasting model 2002-OBE) was 317 Torr for 16 mL volume, the quantity of H_2 is evaluated to 1.4×10^{-4} mol. The corresponding charge consumed during the electrolysis was 28.3 C that amounts to a yield greater than 95% for the HER. Electrolysis performed at $\eta = 200$ mV consumes 728.4 C, yielding a turnover number of 1.2×10^5 after 5 h (or turnover frequency = 6.7 s^{-1}) when the experiment was deliberately stopped. It is rewarding that such a remarkable result could be obtained using a very tiny amount of catalyst. Furthermore, no loss of electrode activity was observed during this electrolysis and even for longer duration. It is worth noting that whichever the η value in the cited range, the electrode remains remarkably stable. With decreasing η, the consumed charge in a given duration decreases as expected, but high turnovers for hydrogen production are still achieved. For example, even with $\eta = 0$ mV, a turnover of 1.7×10^3 is obtained in 24 h.

To our knowledge, the present work reports the first example in which noble metal-free POM-based materials show a turnover frequency (TOF) as high as ca. 6.7 s^{-1} with $\eta = 200$ mV for the HER in aqueous medium. These values compare well with biomimetic nickel complexes covalently attached[54] or physisorbed[55] on carbon nanotubes. Higher TOFs were reported for some bioinspired HER electrocatalysts.[56] However, such performances were obtained in organic or hydro-organic media with usually η values larger than 200 mV.

Tentatively, the following mechanistic pathway can be proposed, which takes into account the main experimental observations.

First wave:

$$\mathrm{POMOF} + 2e^- + 2H^+ \rightleftarrows H_2\mathrm{POMOF}$$

Second wave:

$$H_2\mathrm{POMOF} + 2e^- + 2\{Li(H_2O)_n\}^+ \rightleftarrows [Li_2(H_2O)_{2n}\mathrm{POMOF}] + H_2$$

$$[Li_2(H_2O)_{2n}\mathrm{POMOF}] + 2H^+(\text{Grotthuss type proton hopping}) \rightleftarrows H_2\mathrm{POMOF} + 2\{Li(H_2O)_n\}^+$$

Work in progress will focus on the elaboration of POMOF-based membrane electrodes assemblies.

CONCLUSION

A new family of electroactive POMOFs catalysts for hydrogen evolution reaction (HER) has been evidenced. First, this work confirms that the $\{\varepsilon\text{-}PMo^{V}_{8}Mo^{VI}_{4}O_{36}(OH)_4Zn_4\}$ POM is a versatile and powerful building block for the construction of POMOF structures. By slightly varying the experimental conditions, three POM building blocks, monomeric, dimeric, or chain-like, have been isolated and connected by trimesate linkers. Among them, $\boldsymbol{\varepsilon}(\mathbf{trim})_{4/3}$ exhibits an interesting and previously unreported (3,4)-connected topology, named **ofp**, possessing a 3D open-framework with channels filled here by TBA counterions. A rationale for its favored stabilization over alternative polymorphs is proposed, highlighting a structure directing role of TBA molecules in the assembly of the POM building blocks of $\boldsymbol{\varepsilon}(\mathbf{trim})_{4/3}$. The main challenge remains the synthesis of a porous material. Three strategies are proposed and will be attempted: (i) the replacement of Zn^{II} by M^{III} (M = Ru, Co) cations, which would increase the positive charge on the POM unit and avoid the presence of the TBA counterions, (ii) in the same respect, neutral linker such as bipyridine or pyrazine will lower the overall charge, and (iii) the use of less bulky template such as organoammonium cations with shorter alkyl chains. Second, the $\boldsymbol{\varepsilon}(\mathbf{trim})_{4/3}$ and $[\boldsymbol{\varepsilon}(\mathbf{trim})]_\infty$-based electrodes show remarkable behaviors vis-à-vis the HER. The fact that their performances exceed those of platinum might be attributed both to the structure of the POMOF and to the confinement effect. Even though predicted on theoretical grounds, this last phenomenon has received little experimental confirmation. The electrocatalytic properties of these POMOFs indicate that neither extensive porosity nor the presence of conjugated ligands connecting the POMs are required for the occurrence of outstanding HER properties. This unique feature of POMOFs to allow the stabilization of electroactive POMs in MOF-type scaffold opens up promising perspectives for the design of more efficient catalysts.

ASSOCIATED CONTENT

Supporting Information. Comparison of the simulated and experimental placement in Z-POMOF1, chronoamperometric current variations of $\boldsymbol{\varepsilon}(\mathbf{trim})_{4/3}$/CPE, ball-and-stick representation with partial atomic labeling scheme, selected bond distances and bond valence summations (BVS), projection along the *b* axis of $\boldsymbol{\varepsilon}(\mathbf{trim})_{4/3}$ showing the presence of channels, comparison of the experimental X-ray powder patterns and of the powder patterns calculated from the structure solved from single-crystal X-ray diffraction data, thermal powder diffraction patterns, infrared spectra, comparison of the tilings for **ofp**, **bor**, and **ctn**, suggested scheme for the templating and space filling role of TBA in the as-synthesized $\boldsymbol{\varepsilon}(\mathbf{trim})_{4/3}$, variation of the peak current intensity observed with $\boldsymbol{\varepsilon}_2(\mathbf{trim})_2$/CPE as a function of scan rate, superposition of the 1st and 1200th cyclic voltammograms recorded with $\boldsymbol{\varepsilon}(\mathbf{trim})_{4/3}$/CPE at a scan rate of 100 mV s^{-1}, cyclic voltammogram featuring cesium cation effect on $\boldsymbol{\varepsilon}(\mathbf{trim})_{4/3}$/CPE, cyclic voltammograms observed for $\boldsymbol{\varepsilon}(\mathbf{trim})_{4/3}$/CPE highlighting the insertion of lithium ion on the second wave, and mass spectrum of gas generated by electrolysis.

This material is available free of charge via the Internet at http://pubs.acs.org.

AUTHOR INFORMATION

Corresponding Author

c.mellot-draznieks@ucl.ac.uk; bineta.keita@lcp.u-psud.fr; dolbecq@chimie.uvsq.fr

REFERENCES

(1) Special issue on metal organic frameworks: *Chem. Soc. Rev.* **2009**, *38*, 1201−1508. (b) Rao, C. N. R.; Cheetham, A. K.; Thirumurugan, A. *J. Phys.: Condens. Matter* **2008**, *20*, 083202.

(2) Dolbecq, A.; Dumas, E.; Mayer, C. R.; Mialane, P. *Chem. Rev.* **2010**, *110*, 6009.

(3) (a) Clemente-Juan, J. M.; Coronado, E. *Coord. Chem. Rev.* **1999**, *193*−*195*, 361. (b) Kortz, U.; Müller, A.; van Slageren, J.; Schnacke, J.; Dalal, N. S.; Dressel, M. *Coord. Chem. Rev.* **2009**, *253*, 2315. (c) Mialane, P.; Dolbecq, A.; Sécheresse, F. *Chem. Commun.* **2006**, 3477. (d) Kögerler, P.; Tsukerblat, B.; Müller, A. *Dalton Trans.* **2010**, *39*, 21.

(4) Keita, B.; Nadjo, L. Electrochemistry of Polyoxometalates. In *Encyclopedia of Electrochemistry*; Bard, A. J., Stratmann, M., Eds.; Wiley-VCH: New York, 2006; Vol. 7, p 607.

(5) Special issue on polyoxometalates: Hill, C. L., Ed. *J. Mol. Catal. A* **2007**, *262*, 1−242.

(6) (a) Thiel, J.; Ritchie, C.; Streb, C.; Long, D.-L.; Cronin, L. *J. Am. Chem. Soc.* **2009**, *131*, 4180. (b) Ritchie, C.; Streb, C.; Thiel, J.; Mitchell, S. G.; Miras, H. N.; Long, D.-L.; Boyd, T.; Peacock, R. D.; McGlone, T.; Cronin, L. *Angew. Chem., Int. Ed.* **2008**, *47*, 6881.

(7) Mitchell, S. G.; Streb, C.; Miras, H. N.; Boyd, T.; Long, D. L.; Cronin, L. *Nature Chem.* **2010**, 308.

(8) Queen, W. L.; Hwu, S.-J.; Reighard, S. *Inorg. Chem.* **2010**, *49*, 1316.

(9) (a) Loy, D. A.; Shea, K. J. *Chem. Rev.* **1995**, *95*, 1431. (b) Ribot, F.; Sanchez, C. *Comments Inorg. Chem.* **1999**, *20*, 327. (c) Corriu, J. P. *Eur. J. Inorg. Chem.* **2001**, 1109.

(10) (a) Férey, G.; Mellot-Draznieks, C.; Serre, C.; Millange, F. *Acc. Chem. Res.* **2005**, *38*, 217. (b) Rosseinsky, M. J. *Microporous Mesoporous Mater.* **2004**, *73*, 15. (c) Maspoch, D.; Ruiz-Molina, D.; Veciana, J. *Chem. Soc. Rev.* **2007**, *36*, 770. (d) Rowsell, J. L. C.; Yaghi, O. M. *Microporous Mesoporous Mater.* **2004**, *73*, 3. (e) James, S. L. *Chem. Soc. Rev.* **2003**, *32*, 276. (f) Yaghi, O. M.; O'Keefe, M.; Ockwig, N. W.; Chae, H. K.; Eddaoudi, M.; Kim, J. *Nature* **2003**, *423*, 705. (g) Cheetham, A. K.; Rao, C. N. R.; Feller, R. K. *Chem. Commun.* **2006**, 4780.

(11) (a) Streb, C.; Ritchie, C.; Long, D.-L.; Kögerler, P.; Cronin, L. *Angew. Chem., Int. Ed.* **2007**, *46*, 7579. (b) Zheng, S.-T.; Zhang, J.; Yang, G.-Y. *Angew. Chem., Int. Ed.* **2008**, *47*, 3909.

(12) Coronado, E.; Gimenez-Saiz, C.; Gómez-García, C. J. *Coord. Chem. Rev.* **2005**, *249*, 1776.

(13) Casañ-Pastor, N.; Gómez-Romero, P. *Front. Biosci.* **2004**, *9*, 1759.

(14) Yang, L.; Kinoshita, S.; Yamada, T.; Kanda, S.; Kitagawa, H.; Tokunaga, M.; Ishimoto, T.; Ogura, T.; Nagumo, R.; Miyamoto, A.; Koyama, M. *Angew. Chem., Int. Ed.* **2010**, *49*, 5348.

(15) (a) Burkholder, E.; Golub, V.; O'Connor, C. J.; Zubieta, J. *Inorg. Chem.* **2003**, *42*, 6729. (b) An, H.-Y.; Wang, E.-B.; Xiao, D.-R.; Li, Y.-G.; Su, Z.-M.; Xu, L. *Angew. Chem., Int. Ed.* **2006**, *45*, 904. (c) Han, J. W.; Hill, C. L. *J. Am. Chem. Soc.* **2007**, *129*, 15094. (d) Sha, J.; Peng, J.; Pang, H.; Tian, A.; Chen, J.; Zhang, P.; Zhu, M. *Solid State Sci.* **2008**, *10*, 1491. (e) Yu, F.; Kong, X.-J.; Zheng, Y.-Y.; Ren, Y.-P.; Long, L.-S.; Huang, R.-B.; Zheng, L.-S. *Dalton Trans.* **2009**, 9503.

(16) An, H.-Y.; Wang, E.-B.; Xiao, D.-R.; Li, Y.-G.; Su, Z.-M.; Xu, L. *Angew. Chem., Int. Ed.* **2006**, *45*, 904.

(17) Wang, X.-L.; Li, Y.-G.; Lu, Y.; Fu, H.; Su, Z.-M.; Wang, E. *Cryst. Growth Des.* **2010**, *10*, 4227.

(18) Sha, J.; Peng, J.; Pang, H.; Tian, A.; Chen, J.; Zhang, P.; Zhu, M. *J. Solid State Chem.* **2008**, *10*, 1491.

(19) (a) Yu, F.; Kong, X.-J.; Zheng, Y.-Y.; Ren, Y.-P.; Long, L.-S.; Huang, R.-B.; Zheng, L.-S. *Dalton Trans.* **2009**, 9503. (b) Wang, X.; Hu, H.; Tian, A.; Lin, H.; Li, J. *Inorg. Chem.* **2010**, *49*, 10299.

(20) Mialane, P.; Dolbecq, A.; Lisnard, L.; Mallard, A.; Marrot, J.; Sécheresse, F. *Angew. Chem., Int. Ed.* **2002**, *41*, 2398.

(21) (a) Dolbecq, A.; Mialane, P.; Lisnard, L.; Marrot, J.; Sécheresse, F. *Chem.-Eur. J.* **2003**, *9*, 2914. (b) Dolbecq, A.; Mellot-Draznieks, C.; Mialane, P.; Marrot, J.; Férey, G.; Sécheresse, F. *Eur. J. Inorg. Chem.* **2005**, 3009.

(22) Lei, C.; Mao, J.-G.; Sun, Y.-Q.; Song, J.-L. *Inorg. Chem.* **2004**, *43*, 1964.

(23) Wang, W.; Xu, L.; Gao, G.; Liu, L.; Liu, X. *CrystEngComm* **2009**, *11*, 2488.

(24) Rodriguez-Albelo, L. M.; Ruiz-Salvador, A. R.; Sampieri, A.; Lewis, D. W.; Gómez, A.; Nohra, B.; Mialane, P.; Marrot, J.; Sécheresse, F.; Mellot-Draznieks, C.; Ngo Biboum, R.; Keita, B.; Nadjo, L.; Dolbecq, A. *J. Am. Chem. Soc.* **2009**, *131*, 16078.

(25) Rodriguez-Albelo, L. M.; Ruiz-Salvador, A. R.; Lewis, D. L.; Gómez, A.; Mialane, P.; Marrot, J.; Dolbecq, A.; Sampieri, A.; Mellot-Draznieks, C. *Phys. Chem. Chem. Phys.* **2010**, *12*, 8632.

(26) We use here the database designed for easily classifying known nets, giving each net its own three letter designation (RCSR website http://rcsr.anu.edu.au), see: O'Keeffe, M.; Peskov, M. A.; Ramsden, S. J.; Yaghi, O. M. *Acc. Chem. Res.* **2008**, *41*, 1782.

(27) Abrahams, B. F.; Batten, S. R.; Hamit, H.; Hoskins, B. F.; Robson, R. *Angew. Chem., Int. Ed. Engl.* **1996**, *35*, 1690.

(28) Zhang, Q.; Liu, Y.; Bu, X.; Wu, T.; Feng, P. *Angew. Chem., Int. Ed.* **2008**, *47*, 113.

(29) Hao, Z.-M.; Guo, C.-H.; Wu, H.-S.; Zhang, X.-M. *CrystEngComm* **2010**, *12*, 55.

(30) El-Kaderi, H. M.; Hunt, J. R.; Mendoza-Cortes, J. L.; Côté, A. P.; Taylor, R. E.; O'Keeffe, M.; Yaghi, O. M. *Science* **2007**, 316.

(31) (a) Yaghi, O. M.; O'Keeffe, M.; Ockwig, N. W.; Chae, H. K.; Eddaoudi, M.; Kim, J. *Nature* **2003**, *423*, 705. (b) Ockwig, N. W.; Delgado-Friedrichs, O.; O'Keeffe, M.; Yaghi, O. M. *Acc. Chem. Res.* **2005**, *38*, 176.

(32) (a) Mellot-Draznieks, C.; Dutour, J.; Férey, G. *Z. Anorg. All. Chem.* **2004**, *630*, 2599. (b) Mellot-Draznieks, C.; Férey, G. *Prog. Solid State Sci.* **2005**, *33*, 187.

(33) Mellot-Draznieks, C. *J. Mater. Chem* **2007**, *41*, 4348.

(34) Lewis, L. W.; Ruis-Salvador, A. R.; Gomez, A.; Rodriguez-Albelo, L. M.; Coudert, F. X.; Slater, S.; Cheetham, A. K.; Mellot-Draznieks, C. *CrystEngComm* **2009**, *11*, 2272.

(35) Sheldrick, G. M. *SADABS; program for scaling and correction of area detector data*; University of Göttingen: Germany, 1997.

(36) Blessing, R. *Acta Crystallogr.* **1995**, *A51*, 33.

(37) Sheldrick, G. M. *SHELX-TL version 5.03, Software Package for the Crystal Structure Determination*; Siemens Analytical X-ray Instrument Division: Madison, WI, 1994.

(38) van der Sluis, P.; Spek, A. L. *Acta Crystallogr., Sect. A* **1990**, *46*, 194.

(39) (a) Dybtsev, D. N.; Chun, H.; Kim, K. *Chem. Commun.* **2004**, 1594. (b) Delgado-Friedrichs, O.; O'Keeffe, M.; Yaghi, O. M. *Acta Crystallogr., Sect. A* **2006**, *62*, 350.

(40) Rappé, A. K.; Casewit, C. J.; Colwell, K. S.; Goddard, W. A., III; Skiff, W. M. *J. Am. Chem. Soc.* **1992**, *114*, 10024.

(41) Rappé, A. K.; Goddard, W. A., III. *J. Phys. Chem.* **1995**, *95*, 3358.

(42) Dauger-Osguthorpe, P.; Roberts, V. A.; Osguthorpe, D. J.; Wolff, J.; Genest, M.; Hagler, A. T. *Proteins: Struct., Funct., Genet.* **1988**, *4*, 21.

(43) Materials Studio suite of Software, Accelrys, San Diego, CA.

(44) Keita, B. Method for preparing an electrode for producing hydrogen. PCT Int. Appl., Centre National de la Recherche Scientifique (C.N.R.S.) patent, Chemical Indexing Equivalent to 152:536974 (FR), A1 20100514, 2010.

(45) Levi, M. D.; Markevich, E.; Aurbach, D. *Electrochim. Acta* **2005**, *51*, 98.

(46) Müller, A.; Meyer, J.; Krickemeyer, E.; Diemann, E. *Angew. Chem., Int. Ed. Engl.* **1996**, *35*, 1206.

(47) Spek, A. L. *J. Appl. Crystallogr.* **2003**, *36*, 7.
(48) Henson, N.; Cheetham, A. K.; Gale, J. D. *Chem. Mater.* **1994**, *6*, 147.
(49) Lee, C.; Mellot-Draznieks, C.; Slater, B.; Wu, G.; Harrison, W. T. A.; Rao, C. N. R.; Cheetham, A. K. *Chem. Commun.* **2006**, 2687.
(50) (a) Keita, B.; Nadjo, L. *J. Mol. Catal. A* **2007**, *262*, 190.(b) Hill, C. L., Guest Ed. *Chem. Rev.* **1998**, *98*, 1−389.
(51) (a) Albery, W. L.; Hillman, A. R. *Annu. Rep. C* **1982**, *78*, 377. (b) Anson, F. C.; Savéant, J. M.; Shigehara, K. *J. Am. Chem. Soc.* **1983**, *105*, 1096 and references therein. (c) Anson, F. C.; Savéant, J. M.; Ohsaka, T. *J. Am. Chem. Soc.* **1983**, *105*, 4883 and references therein.
(52) (a) Keita, B.; Nadjo, L. Electrochemical reactions on modified electrodes. In *Encyclopedia of Electrochemistry*; Bard, A. J., Stratmann, M., Eds.; Wiley-VCH: Weinheim, Germany, 2007; Vol. 11, pp 685−728. (b) Keita, B.; Kortz, U.; Brudna Holzle, L. R.; Brown, S.; Nadjo, L. *Langmuir* **2007**, *23*, 9531 and references therein.
(53) Chen, J.; Huang, J.; Swiegers, G. F.; Too, C. O.; Wallace, G. G. *Chem. Commun.* **2004**, 308.
(54) Le Goff, A.; Artero, V.; Jousselme, B.; Tran, P. D.; Guillet, N.; Métayé, R.; Fihri, A.; Palacin, S.; Fontecave, M. *Science* **2009**, *326*, 1384.
(55) Tran, P. D.; Le Goff, A.; Heidkamp, J.; Jousselme, B.; Guillet, N.; Palacin, S.; Dau, H.; Fontecave, M.; Artero, V. *Angew. Chem., Int. Ed.* **2011**, *50*, 1371.
(56) (a) Jain, A.; Lense, S.; Linehan, J. C.; Raugei, S.; Cho, H.; DuBois, D. L.; Shaw, W. *J. Inorg. Chem.* **2011**, *50*, 4073–4085. (b) DuBois, D. L.; Bullock, R. M. *Eur. J. Inorg. Chem.* **2011**, 1017–1027.